

Article

Lab-Scale X-Ray Exposure Has No Measurable Impact on Lithium-Ion Battery Performance and Lifetime

Jinhong Min, Amariah Condon and Peter M. Attia *

Glimpse Engineering Inc., 444 Somerville Avenue, Somerville, MA 02143, USA

* Correspondence: peter.m.attia@gmail.com

Abstract: X-ray characterization is broadly used in battery research, development, manufacturing, and quality control. However, the impact of lab-scale X-ray exposure on battery performance and lifetime is not well understood. In this work, we evaluate the impact of lab-scale X-rays on battery performance and lifetime. We tested groups of cylindrical 18,650 cells using 2 min and 60 min X-ray imaging conditions; the performance and lifetime of these cells were identical to a control group without X-ray exposure. These results suggest that lab-scale X-ray characterization is safe for lithium-ion batteries.

Keywords: lithium-ion batteries; X-ray imaging; beam damage; computed tomography

1. Introduction

X-ray characterization techniques are broadly used throughout battery research and development (R&D), as well as manufacturing [1–5]. Specifically, both 2D X-ray imaging and 3D X-ray imaging (computed tomography, or CT) techniques are commonly employed for cell-level characterization to understand swelling and defect evolution over life [6–23], cell manufacturing to assess quality (both the presence of defects and conformance to the design) [3–5,24,25], and failure analysis to root cause failures in the field [26].

Despite the centrality of these techniques throughout the battery value chain, the impact of X-ray exposure on battery performance—specifically, X-ray exposure from lab sources, as opposed to synchrotrons—is not well understood. Here, we adapt the commonly used term “lab scale” to refer to any non-synchrotron X-ray source, even though these sources are used in both lab and production settings in the battery industry. The X-ray imaging of human patients can damage the DNA and thus increase the risk of cancer. As such, clinicians attempt to minimize X-ray exposure during medical imaging procedures [27,28]. While battery cells certainly do not suffer from the same damage mechanisms as humans, batteries contain many sensitive components such as electrolytes and interphasial [29] layers. In fact, battery electrolytes and positive electrode materials have been shown to degrade upon exposure to gamma rays [30–33], and the interphasial layer of the graphitic negative electrode is notoriously difficult to characterize due to its sensitivity to oxygen, water, and electromagnetic radiation [34–40]. Furthermore, a wide body of literature [41–49] has demonstrated that synchrotron X-ray exposure can both hinder electrochemical reactions during operando battery studies and damage the crystalline structure of battery materials. Understanding the electrochemical impact of lab-scale X-ray exposure on key battery performance metrics is important to design both R&D test plans and inspection strategies for quality control.

In this work, we evaluated the impact of lab-scale X-ray exposure on lithium-ion battery performance and lifetime. We tested three groups of cylindrical 18,650 cells: cells



Academic Editors: Douglas Ivey and Lei Mao

Received: 17 December 2024

Revised: 21 January 2025

Accepted: 7 February 2025

Published: 11 February 2025

Citation: Min, J.; Condon, A.; Attia, P.M. Lab-Scale X-Ray Exposure Has No Measurable Impact on Lithium-Ion Battery Performance and Lifetime. *Batteries* **2025**, *11*, 73. <https://doi.org/10.3390/batteries11020073>

Copyright: © 2025 by the authors. Licensee MDPI, Basel, Switzerland. This article is an open access article distributed under the terms and conditions of the Creative Commons Attribution (CC BY) license (<https://creativecommons.org/licenses/by/4.0/>).

exposed to realistic X-ray doses for two minutes, cells exposed to realistic X-ray doses for sixty minutes, and a control group that was not exposed to X-rays. We tested both their performance and their lifetime after this lab-scale X-ray exposure. In short, we found no statistically significant differences between the three experimental groups. Our results suggest that practical doses of lab-scale X-ray exposure are likely safe for most battery characterization use cases.

2. Materials and Methods

We used EVE INR18650-33V cells (EVE Energy Co., Huizhou, China) for this study. These NMC/graphite cells were selected due to their low geometrical variability, as observed in the dataset presented in Condon et al.'s work [5].

Each cell was individually scanned using the Nikon XT H 225 ST 2x system (Nikon Metrology Inc., Brighton, MI, USA). This system was equipped with a 225 kV rotating anode X-ray source. We selected a 225 kV X-ray source as sources with this beam voltage are common in industrial CT systems; however, it is worth noting that the rotating anode X-ray source was approximately three times brighter than conventional lab-scale X-ray sources and thus represented the upper limit of the expected X-ray dose in this setting. The beam voltage and beam current were 210 kV and 190 μ A, respectively. Data acquisition was performed using Nikon's Inspect-X software (version XT 6.12). All fresh cell scans were performed at shipping voltage; all aged cell scans were performed at 2.5 V.

All electrochemical tests were performed on a Neware BTS4000-5V6A cycler system (Neware Technology Limited, Shenzhen, China).

The RPT test consisted of three consecutive constant charge and discharge cycles. In the first cycle, the cells were charged at a constant current of 155 mA (C/20) until they reached a cutoff voltage of 4.2 V and then discharged at 155 mA to a cutoff voltage of 2.5 V. In the second cycle, the cells were charged at 620 mA (C/5) to 4.2 V and then discharged at 620 mA to 2.5 V. In the third cycle, the cells were charged at 1550 mA (C/2) to 4.2 V and then discharged at 1550 mA to 2.5 V. A 5 min rest period was included between each cycle. The tests were conducted in convection-based temperature chambers set to 33 °C; conventionally, RPTs are performed at, or slightly above, room temperature to understand the state of the cell in field-representative conditions. An example of an RPT test is shown in Supplementary Figure S1.

For the cycling tests, all cells were charged at a constant current of 1550 mA (C/2) until they reached a cutoff voltage of 4.2 V, after which the voltage was held until the charging current dropped to 62 mA. Discharging was conducted at a constant current of 3100 mA (1C) until the cells reached a cutoff voltage of 2.5 V. Cycling tests were performed in convection-based temperature chambers set to 45 °C to accelerate cell aging.

Fifteen cells were placed into one of three experimental groups for a total of five cells per group. The three experimental groups were the following:

1. No X-ray exposure (control group);
2. Two-minute X-ray exposure;
3. Sixty-minute X-ray exposure.

We selected the 2 min X-ray exposure time since this scan time was used in the rapid CT scans in Condon et al.'s work [5], and we selected the 60 min X-ray exposure time as both a representative value for conventional CT scans and an extreme upper bound of practical test times in the battery production setting. It is worth noting that 2D X-ray imaging, which is more commonly used in battery production than CT today, typically uses exposures ranging from 100 to 1000 ms, and thus the X-ray doses used in this experiment were at least 100× larger than those used in typical 2D X-ray imaging in a battery production environment.

The test plan for all experimental groups was the following:

1. First RPT;
2. X-ray exposure for the two-minute and sixty-minute experimental groups (this step was skipped for the control group);
3. Second RPT;
4. Cycling for 300 cycles;
5. Final RPT;
6. Two-minute CT scan.

A flowchart visualizing the experimental procedure is displayed in Figure A1 (Appendix A).

3. Results

First, we characterized all fifteen cells via an initial RPT. Figure 1 displays the RPT data. We observed that the initial variability between cells was low, which made these cells good candidates for this study (i.e., we could safely neglect cell-to-cell variability and focus on the effects of X-ray exposure).

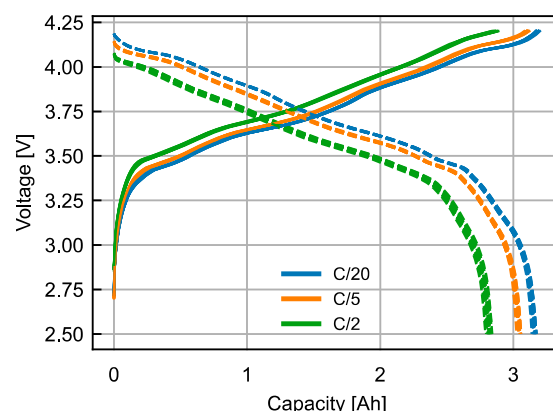


Figure 1. Voltage vs. capacity for all fifteen cells used in this study during their first RPT. The data for all three C rates in the RPT are displayed. Charging is represented by solid lines, while discharging is represented by dashed lines. The inter-cell variability is minimal.

We then split the cells into three experimental groups, exposed them to X-rays, performed another RPT, and cycled the cells for 300 cycles with an aggressive cycling protocol (see Section 2). Figure 2 displays discharge capacity vs. cycle number for the three experimental groups. No substantial differences in capacity retention were observed between the three experimental groups.

After this cycling test, we performed a final RPT. Figure 3 displays a comparison of discharge capacity between the three RPTs (pre exposure, post exposure/pre cycling, and finally post cycling) at the three C rates used in the RPT (C/20, C/5, and C/2). We also quantified the probabilities (p values) that differences between all rates and all groups across RPTs would be statistically significant ($p < 0.05$) using two-sample T tests. The voltage vs. capacity data for these RPTs are displayed in Supplementary Figures S2 and S3.

After this final RPT, we performed two-minute CT scans of all cells. We did not detect any differences between the experimental groups via visual inspection (Supplementary Figure S4). We then quantified the core area of all scans. In cylindrical cells, the jellyroll swells both inwards (towards the core) and outwards (towards the can) during aging; since the jellyroll can more easily expand into the empty core than the rigid can, the decrease in core area with respect to time can thus serve as a proxy for swelling in cylindrical cells [11,18,23]. Figure 4 displays a comparison of the core area before and after the cycling experiment across all three experimental groups. Again, no significant differences

were observed between the experimental groups as quantified via the two-sample T tests ($p = 0.529$) and the 95% confidence intervals (-0.447 mm^2 and 0.106 mm^2).

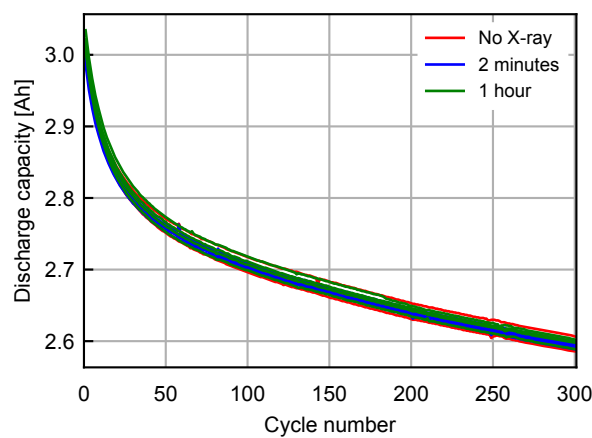


Figure 2. Discharge capacity vs. cycle number during the cycling experiment for all fifteen cells. No substantial differences in capacity retention are observed between the three experimental groups.

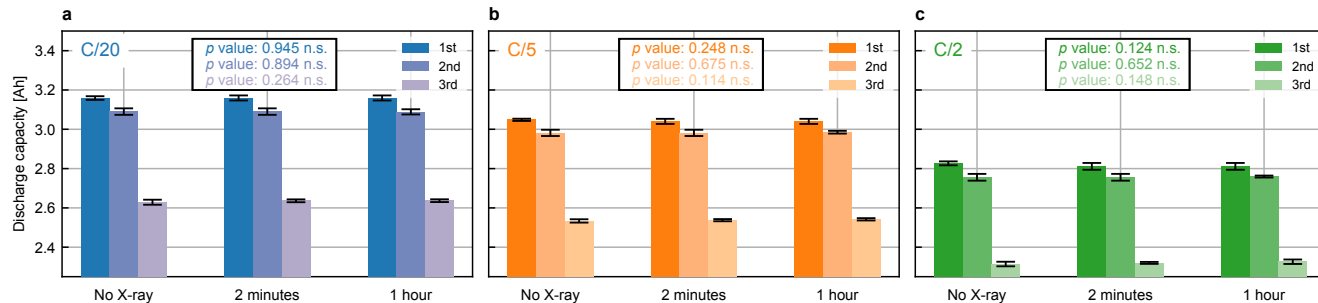


Figure 3. Discharge capacity comparison between all three experimental groups (x axis) and across all three RPTs (color axis): (a) C/20 discharge capacity; (b) C/5 discharge capacity; and (c) C/2 discharge capacity. The p values represent the probability that the differences between the control group and the 1 h exposure group (in principle, the most extreme differences) are due to chance; we consider $p < 0.05$ a statistically significant result. We did not observe any statistically significant differences between the experimental groups.

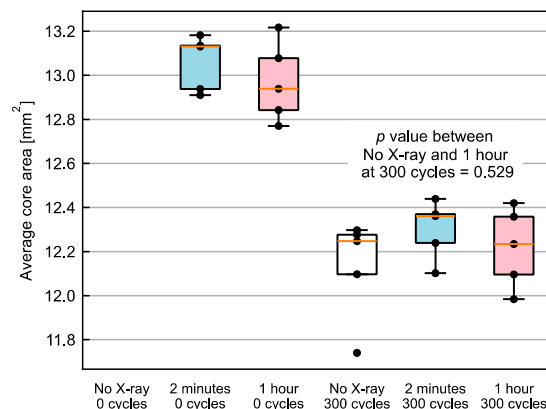


Figure 4. Core area comparison between all three experimental groups. Each group is visualized via a box-and-whisker plot, in which the orange line represents the median value, the bottom and top edges of the box represent the first and third quartiles, respectively, and the whiskers extend from the box to the farthest data point lying within $1.5 \times$ the inter-quartile range from the box. Each point represents the core area averaged across the height of the cell. The core area was obtained from the initial CT scan (not available for the control group) and the CT scan of the cells after the final RPT. No significant differences in core area were observed between the experimental groups after the cycling test, as quantified via the two-sample T tests ($p = 0.529$) and 95% confidence intervals (-0.447 mm^2 and 0.106 mm^2) between the control group and the 1 h exposure group.

4. Discussion

The results of this study are unambiguous: under the conditions used here, X-ray exposure has no statistically significant impact on energy, rate, lifetime, or swelling (in our view, the most important performance parameters in lithium-ion batteries). We discuss this result in the remainder of this section.

First, we calculated the exposed dose for these cells. We present the detailed calculations, via two methods, in Appendix B. Both methods converged to a value around ~ 10 Gy (1 Gy = 1 Gray = 1 J kg⁻¹) for the two-minute exposure group and ~ 300 Gy for the sixty-minute exposure group. For context, 8 Gy is considered a lethal dose of absorbed radiation in humans [50].

While we calculated the exposed dose in this study, the more relevant metric for beam damage is the absorbed dose. Upon X-ray exposure, only the absorbed X-rays cause damage; the transmitted X-rays have no effect. Unfortunately, the absorbed dose is difficult to estimate from first principles due to the multi-material object and the polychromatic beam. We roughly estimated the absorbed dose to be approximately 60% of the exposed dose based on X-ray absorption simulations (Appendix C, Table A1, Figure A2), so the absorbed X-ray doses would be ~ 6 Gy for the two-minute exposure group and ~ 180 Gy for the sixty-minute exposure group. Of the total X-rays absorbed, 31% was absorbed by the electrochemically active components (carbon and LiNiMnCoO₂); of this fraction, 82% was absorbed by the LiNiMnCoO₂. Fortunately, from a beam damage standpoint, the battery components with the highest radiodensity (e.g., the stainless steel can, the copper current collector) tend to be inactive. Lastly, it is worth noting that industrial X-ray imaging typically uses X-rays with a higher energy compared to medical X-ray imaging (since industrial imaging typically involves imaging samples of a higher radiodensity), leading to less X-ray absorption (all else being equal).

Our results may seem surprising in light of the previously cited studies indicating the sensitivity of electrolyte [30,32,33], positive electrode [31,33], and interphasial layers [34–40] to electromagnetic radiation, as well as the wide body of literature suggesting that synchrotron X-ray exposure can induce temporary or permanent beam damage [41–49]. We hereby discuss these results in light of our own, one by one. The key factors that we considered in this study were the X-ray dose and the X-ray energy.

First, we examined the reports of the sensitivity of electrolyte and positive electrode to gamma rays [30–33]. In these studies, the dose was typically in the order of 5–100 kGy, which was much higher than the maximum dose used in this study. Additionally, it is worth noting that gamma rays are more likely to induce radiolysis in organic compounds than X-rays. Radiolysis was the prevalent damage mechanism for electrolytes reported in these studies, and, thus, a dose of X-rays is likely much safer for electrolytes than an equivalent dose of gamma rays.

Second, we evaluated the reports of the well-known sensitivity of interphasial layers—specifically, the solid–electrolyte interphase (SEI) of the negative electrode—to various types of characterization techniques [34–40]. While we were unable to identify a prior report which calculated the X-ray dose during SEI characterization, we noted that the primary reported sensitivities of the SEI were to air and moisture exposure and mechanical damage (exposure to vacuum, sample washing, etc.). To the best of our knowledge, the SEI has not been shown to be damaged upon X-ray exposure in the absence of air and moisture exposure. In fact, the solid-phase inorganic compounds that have been identified in the SEI (typically LiF, Li₂O, Li₂CO₃, etc.), which are believed to provide most of the passivating capabilities of the SEI [35,40], may be quite robust to X-ray exposure.

Third, we addressed the numerous reports [41–49] on the sensitivity of battery material structure and operation to synchrotron X-rays. Specifically, high synchrotron X-ray

exposure can deleteriously modify both the electrochemical activity and the microstructure of battery materials. We summarize this literature in Appendix D and Table A2. In this case, the two risk factors we previously identified—the X-ray dose and the X-ray energies—all had a significantly higher impact than in the synchrotron radiation case. First, the typical X-ray dose reported in these works was, at a minimum, in the order of 1 MGy, or 4–5 orders of magnitude higher than the doses used in our experiment. In fact, some of these reports [48,49] observed no X-ray damage for doses below 1 MGy. These high doses, especially when localized to a small X-ray spot size, could also induce local heating [44–46,49]. Second, the X-ray energies for synchrotron light sources (5–50 keV) were typically lower than the lab sources (10–150 keV); since lower-energy X-rays are more likely to interact with matter than higher-energy X-rays, lower-energy X-rays are more likely to induce beam damage.

Another concern was that high X-ray exposure could heat the cell to extreme temperatures [44] and that high temperatures could cause cell degradation and safety events [51–53]. However, even under the most aggressive assumptions, we found that the cell heating induced by these X-ray doses was negligible. For instance, we assumed that 100% of the exposed dose was absorbed by the cell and that no heat was lost over the course of the experiment. Cylindrical cell heat capacities have been reported to be 1000–2000 J kg⁻¹ K⁻¹ [51,54]; thus, in this study, we assumed a value of 1000 J kg⁻¹ K⁻¹ to model the more aggressive case. Using the simple heat capacity equation $Q = mc\Delta T$, we obtained $\Delta T = Q/mc$. For $Q/m = 300 \text{ J kg}^{-1}$ (the dose assuming 100% absorption for the 60 min scans), $\Delta T = (300 \text{ J kg}^{-1})/(1000 \text{ J kg}^{-1} \text{ K}^{-1}) = 0.3 \text{ K}$, meaning that the worst-case temperature increase over the course of a 1 h scan was negligible. Our measurements of cell temperature during X-ray exposure confirmed this result (Figure S5).

These discussion points aside, we commented on the potential benefits of minimizing the exposed dose. In medical CT imaging, advanced reconstruction techniques are routinely used to minimize patients' X-ray exposure [55]. While battery applications are clearly less sensitive to high X-ray exposure than the clinical case, we still see value in continuously working to decrease exposure to minimize all possible mechanisms of beam damage (aside from the corollary benefit of shorter scan times).

Lastly, we wish to discuss the universality of our results. While the strong conclusions from this simple study indicate that lab-scale X-ray exposure concerns for cell-level battery characterization are likely negligible in practice, we cannot guarantee that these conclusions would hold for other test conditions. For instance, larger batteries such as prismatic cells might require more aggressive X-ray settings per unit mass, while other battery chemistries such as sodium-ion might have more sensitive interphasial layers than lithium-ion, and other cycling conditions may highlight non-zero impacts of high X-ray exposure. Furthermore, despite the lack of any electrochemical differences in the cycling data after 300 cycles (using aggressive cycling conditions), the trends between the experimental groups might diverge after further cycling due to a latent degradation mechanism [56]. That said, both our results and the existing literature [48,49] indicate reason for optimism that practical lab-scale X-ray exposure doses are a non-issue for battery performance and lifetime.

5. Conclusions

In this work, we demonstrated that even the upper practical limit of lab-scale X-ray exposure does not have a statistically significant impact on battery energy, rate, lifetime, or swelling under aggressive cycling conditions. While our results may not hold universally for all cell designs, test/usage conditions, and X-ray exposure, our observation that even high lab-scale X-ray exposure appears safe is an encouraging finding for scientists and engineers interested in the X-ray characterization of batteries.

Supplementary Materials: The following supporting information can be downloaded at <https://www.mdpi.com/article/10.3390/batteries11020073/s1>: Figure S1: Voltage vs. capacity for a single RPT; Figure S2: Voltage vs. capacity comparison between the first and second RPT and across all C rates and experimental groups; Figure S3: Voltage vs. capacity comparison between the first and third RPT; Figure S4: CT images from the middle ($Z = 35$ mm) of representative cells from the 2 min and 1 h exposure groups; and Figure S5: Results of a temperature-monitoring experiment.

Author Contributions: Conceptualization, P.M.A.; methodology, P.M.A.; software, J.M. and P.M.A.; validation, P.M.A.; formal analysis, P.M.A.; investigation, J.M. and A.C.; resources, A.C. and P.M.A.; data curation, A.C.; writing—original draft preparation, P.M.A.; writing—review and editing, J.M., A.C. and P.M.A.; visualization, J.M.; supervision, P.M.A.; and project administration, P.M.A. All authors have read and agreed to the published version of the manuscript.

Funding: This research received no external funding.

Data Availability Statement: All data and code are publicly available on GitHub (<https://github.com/jinhongm-umich/X-ray-influence/>, accessed on 20 January 2025).

Acknowledgments: We thank Jim Sehnert (Glimpse), Till Dreier (Excillum), and Andrew Ramsey (Nikon) for insightful discussions.

Conflicts of Interest: A.C. and P.M.A. have financial interests in Glimpse Engineering Inc., which specializes in high-throughput CT scanning for batteries. J.M., A.C. and P.M.A. were employees of Glimpse Engineering Inc. when this study was conducted.

Abbreviations

The following abbreviations are used in this manuscript:

CT	Computed tomography
R&D	Research and development
RPT	Reference performance test
SEI	Solid–electrolyte interphase
SOD	Source–object distance

Appendix A

A flowchart visualizing the experimental procedure is displayed in Figure A1.

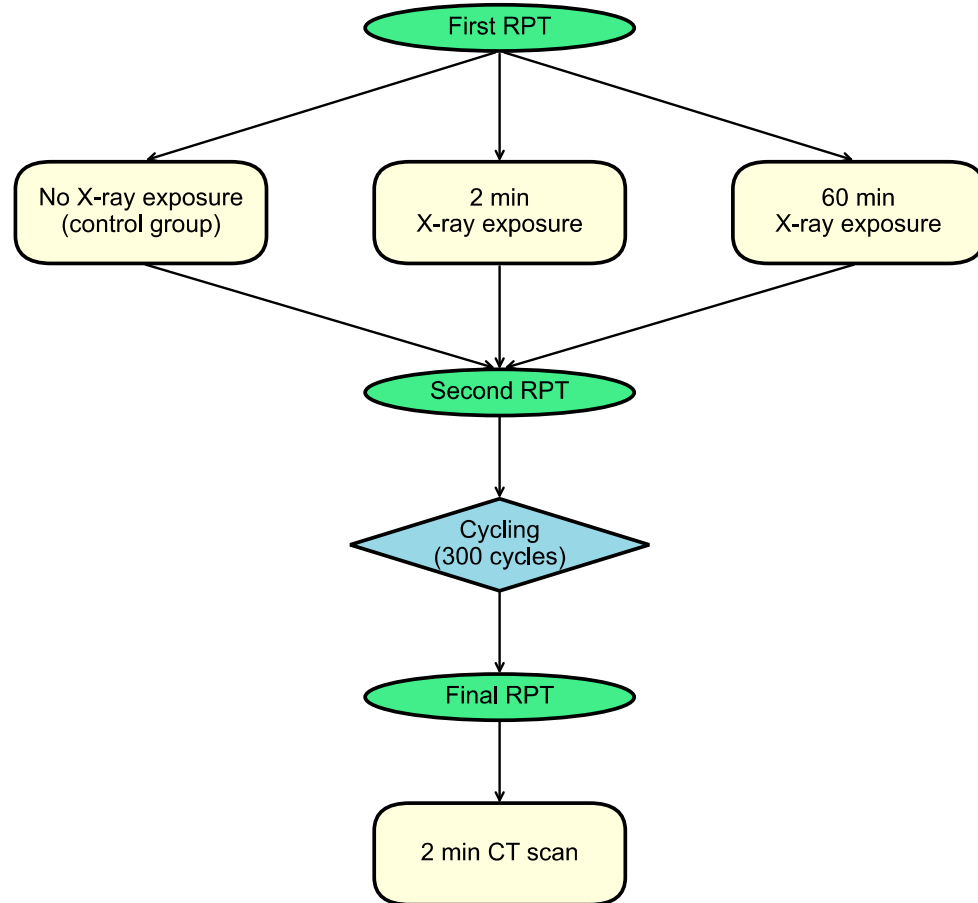


Figure A1. Experimental procedure used in this work. RPTs are displayed as green ellipses, cycling is displayed as a blue diamond, and steps involving X-rays are displayed as yellow rounded rectangles.

Appendix B

We can calculate the exposed dose via two methods.

Appendix B.1

The British Standard 4094, Part 2 provides a chart of X-ray exposure as a function of the tube potential and the filter (Figure 3.2 of reference [57]). For our system (beam potential of ~ 200 kV and a filter of 2.5 mm Al), the exposure rate 1 m from the target was approximately $3 \text{ rad mA}^{-1} \text{ min}^{-1} = 0.03 \text{ Gy mA}^{-1} \text{ min}^{-1}$ (subsequently termed E). To adjust for the true source-object distance (SOD), we used the inverse square law and adjust the exposure rate by $(1000 \text{ mm/SOD})^2$. We then derived the exposed dose, D_{exposed} , to be $E \times (1000 \text{ mm/SOD})^2 \times I_{\text{tube}} \times t_{\text{exposure}}$. Using this equation, the exposed dose was $\sim 10 \text{ Gy}$ for an exposure time of 2 min and $\sim 300 \text{ Gy}$ for an exposure time of 60 min.

Appendix B.2

The power of the X-rays coming out of the source, $P_{X\text{-rays out}}$, is given by the efficiency of electrical energy going in to the energy of the X-rays going out, η , multiplied by the fraction of the dose retained after filtering, ϵ , and the power of the electrical input into the source, $P_{\text{electrical input in}}$:

$$P_{X\text{-rays out}} = \eta \epsilon P_{\text{electrical input in}} \quad (\text{A1})$$

The intensity (flux) of the X-rays at the object, $I_{X\text{-rays at object}}$, is given by the inverse-square law, using the source–object distance, d_{SOD} , as the relevant distance:

$$I_{X\text{-rays at object}} = \frac{P_{X\text{-rays out}}}{4\pi d_{SOD}^2} = \frac{\eta\epsilon P_{electrical\ input\ in}}{4\pi d_{SOC}^2} \quad (\text{A2})$$

This equation is not *strictly* correct as the X-ray intensity will vary from the region of the cell at the centerline of the source to the regions of the cell above/below the centerline of the source (since, technically, the distance from the source to the object is different), but this should be close enough for now.

The power of the X-rays on the object, $P_{X\text{-rays on cell in beam}}$, is given by flux of the X-rays at the SOD, $I_{X\text{-rays at object}}$, multiplied by the area of the cell contained within the X-ray beam, $A_{cell\ in\ beam}$:

$$P_{X\text{-rays on cell in beam}} = A_{cell\ in\ beam} I_{X\text{-rays at object}} = A_{cell\ in\ beam} \frac{\eta\epsilon P_{electrical\ input\ in}}{4\pi d_{SOD}^2} \quad (\text{A3})$$

The area of the cell contained within the X-ray beam, $A_{cell\ in\ beam}$, is the “projection area” of the cell, also known as the area of the cell when viewed in 2D. This area is $d_{cell}h_{cell}$.

We can now rewrite $P_{X\text{-rays on cell in beam}}$ as follows:

$$P_{X\text{-rays on cell in beam}} = A_{cell\ in\ beam} I_{X\text{-rays at object}} = d_{cell}h_{cell} \frac{\eta\epsilon P_{electrical\ input\ in}}{4\pi d_{SOD}^2} \quad (\text{A4})$$

The X-ray energy that irradiates the cell, $E_{X\text{-rays on cell}}$, is given by the power multiplied by the scan time:

$$E_{X\text{-rays on cell}} = P_{X\text{-rays on cell in beam}} t_{scan} = d_{cell}h_{cell} \frac{\eta\epsilon P_{electrical\ input\ in}}{4\pi d_{SOD}^2} t_{scan} \quad (\text{A5})$$

To convert to exposed dose, $D_{exposed}$, we would divide by the cell mass, m_{cell} :

$$D_{exposed} = d_{cell}h_{cell} \frac{\eta\epsilon P_{electrical\ input\ in}}{4\pi d_{SOD}^2 m_{cell}} t_{scan} \quad (\text{A6})$$

Using this equation, we calculated $D_{exposed} \approx 10$ Gy for a two-minute scan and $D_{exposed} \approx 300$ Gy for a sixty-minute scan.

Appendix C

In this Appendix, we estimate the fraction of X-rays absorbed by the cell.

For the purposes of this study, we created a simplified model of a battery that only included the five most significant battery components: steel (iron) for the can, copper as the negative electrode current collector, aluminum as the positive electrode current collector, $\text{LiNi}_{0.8}\text{Mn}_{0.1}\text{Co}_{0.1}\text{O}_2$ for the positive electrode, and carbon for the negative electrode. We estimated the thickness of each major component via measurements of a “radial slice” (Supplementary Figure S4). In our 1D model, we assumed that the battery consisted of the following:

- 200 μm of iron (representing one side of the can);
- Forty electrode stacks, each of which consist of the following:
 - A $\text{LiNi}_{0.8}\text{Mn}_{0.1}\text{Co}_{0.1}\text{O}_2$ -based positive electrode with a single-sided thickness of 60 μm and a porosity of 50% (effective thickness = 30 μm);
 - An aluminum current collector with a single-sided thickness of 10 μm ;

- A LiNi_{0.8}Mn_{0.1}Co_{0.1}O₂-based positive electrode with a single-sided thickness of 60 μm and a porosity of 50% (effective thickness = 30 μm);
- A carbon-based positive electrode with a single-sided thickness of 80 μm and a porosity of 50% (effective thickness = 40 μm);
- A copper current collector with a single-sided thickness of 10 μm ;
- A carbon-based negative electrode with a single-sided thickness of 80 μm and a porosity of 50% (effective thickness = 40 μm);
- 200 μm of iron (representing the other side of the can).

These attributes are detailed in Table A1.

Table A1. Details of the five most significant components for the cell design used in this work. For components in the jellyroll, the thickness per stack refers to the total measurable thickness in a double-sided electrode stack; “ $\times 2$ ” refers to the fact that electrodes are double-sided. The porosity of porous components is assumed to be 50% for all electrode components. In our simulation, we assume that the X-rays first pass through the can, then the 40 electrode stacks, and then the can again. The attenuation at 60 keV is included for reference.

Material	Location	Attenuation at 60 keV (% mm^{-1})	Thickness per Stack (μm)	Porosity (%)
Steel (iron)	Can	61.1%	-	0
Copper	Current collector	75.9%	10	0
Aluminum	Current collector	7.2%	10	0
Carbon	Negative electrode + separator	2.9%	80 \times 2	50
LiNiMnCoO ₂	Positive electrode	36.4%	60 \times 2	50

We then used the SpekPy Python package to simulate X-ray absorption in this system [58]. The results are displayed in Figure A2. The initial spectrum was generated assuming a beam voltage of 210 kV, a beam angle of 40°, and an aluminum filter of 2.5 mm. In Figure A2a, we plot both the original spectrum and the final spectrum after the X-rays have passed through the object. Our model suggested that 74% of the X-rays were absorbed by the object via this 1D model. We also observed the hardening of the X-ray beam after it had passed through the object by the rightward shift in the Bremsstrahlung radiation. In Figure A2b, we visualize the relative absorption of each of the five components. Of the total X-rays absorbed, 31% was absorbed by the electrochemically active components (carbon and LiNiMnCoO₂); of this fraction, 82% was absorbed by the LiNiMnCoO₂.

A final factor to consider was that the path length of X-rays through the object depended on whether the X-rays passed through the thickest cell dimension along the X-ray path (the diameter) or via another path parallel to the cells. In other words, our 1D model overestimated X-ray absorption through a cylindrical battery. Since the average path length through a family of parallel chords in a circle of diameter D is $\pi D/4$, we could approximate the total absorbed fraction to be $\pi/4 \times 73.7\% \approx 58\%$.

This calculation yielded a sensible result for the total fraction of X-rays absorbed by the cell.

Appendix D

A summary of the existing literature on beam damage in battery materials due to synchrotron radiation is presented in Table A2.

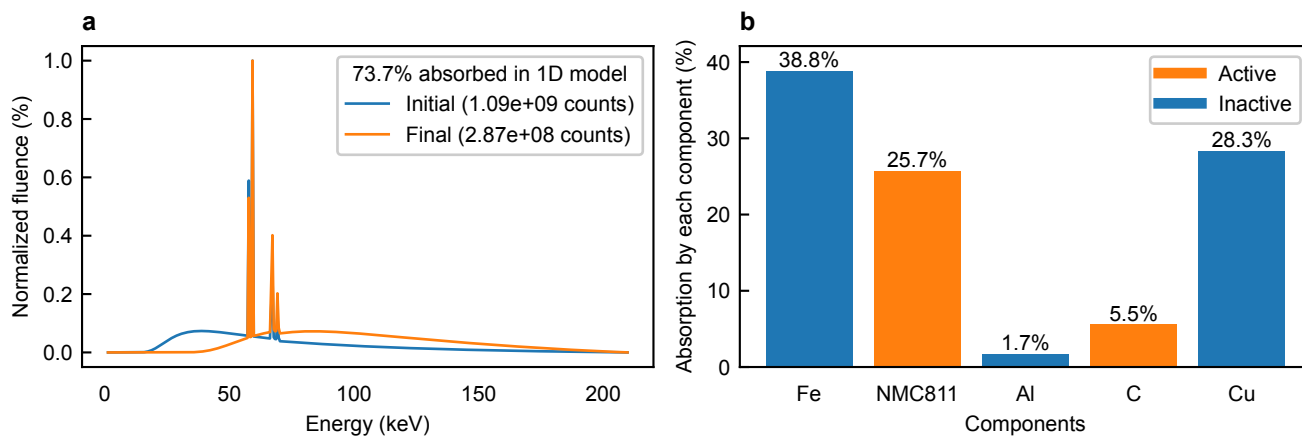


Figure A2. Simulated X-ray absorption in our battery. The simulation was performed using the SpekPy Python package [58]. (a) The original spectrum and the final spectrum after the X-rays have passed through the object, normalized to the maximum value in the spectra. The total fluence is displayed in the legend. From these numbers, we can estimate that 74% of the X-rays were absorbed by the object via this 1D model. We can also observe the hardening of the X-ray beam after it has passed through the object by the rightward shift in the Bremsstrahlung radiation. (b) Relative absorption of each of the five components. Of the total X-rays absorbed, 31% was absorbed by the electrochemically active components (carbon and LiNiMnCoO₂); of this fraction, 82% was absorbed by the LiNiMnCoO₂.

Table A2. Summary of the existing literature on beam damage in battery materials due to synchrotron radiation (with the exception of this work). The electrode material(s) column refers to the primary electrode material under consideration in a given study. The photons/second column reports values rounded to the nearest order of magnitude. The characteristic length column refers to either the spot size in one dimension or the resolution (whichever is reported). The effect column refers to the primary effect observed in the study (either structural damage or reaction hindrance). Entries for which information was not reported by the authors are left blank. The photons/second of our source is unknown.

Authors [Ref]	Electrode Material(s)	Beam Energy (keV)	Photons/Second	Characteristic Length (nm)	Dose (MGy)	Effect	Timescale (Minutes)	Notes
Nelson et al. [41]	Sulfur	6	10^{12}	50		Structural damage	0.75	
Borkiewicz et al. [42]	LFP	17, 58		500		Reaction hindrance		
Lim et al. [43]	Ge _{0.9} Se _{0.1}	11.2	10^{11}	38		Structural damage	4	
Li et al. [45]	Sulfur	7.7	10^{13}	2000		Structural damage	2	
Blondeau et al. [46]	MgInSb	27.9, 30.9	10^{11}	438	1–60	Reaction hindrance	5	
Christensen et al. [47]	LFP, NMC, and graphite	15, 25, 35	10^{11} – 10^{12}	500	Varied	Reaction hindrance	Varied	
Jousseau et al. [48]	NMC and graphite	27	10^{11}	424	1–11	Both	17.5	No effects <80 kGy
Black et al. [49]	NMC and LFP	11, 35	10^{11}	387	Varied	Reaction hindrance	Varied	No effects <1 MGy
This work	NMC and graphite	10–225		16,000	0.01–0.3	None	2–60	

References

1. Pietsch, P.; Wood, V. X-Ray Tomography for Lithium Ion Battery Research: A Practical Guide. *Annu. Rev. Mater. Res.* **2017**, *47*, 451–479. [[CrossRef](#)]
2. Scharf, J.; Chouchane, M.; Finegan, D.P.; Lu, B.; Redquest, C.; Kim, M.; Yao, W.; Franco, A.A.; Gostovic, D.; Liu, Z.; et al. Bridging Nano- and Microscale X-Ray Tomography for Battery Research by Leveraging Artificial Intelligence. *Nat. Nanotechnol.* **2022**, *17*, 446–459. [[CrossRef](#)] [[PubMed](#)]

3. McGovern, M.E.; Bruder, D.D.; Huemiller, E.D.; Rinker, T.J.; Bracey, J.T.; Sekol, R.C.; Abell, J.A. A Review of Research Needs in Nondestructive Evaluation for Quality Verification in Electric Vehicle Lithium-Ion Battery Cell Manufacturing. *J. Power Sources* **2023**, *561*, 232742. [[CrossRef](#)]
4. Attia, P.M.; Moch, E.; Herring, P.K. Challenges and Opportunities for High-Quality Battery Production at Scale. *Nat. Commun.* **2025**, *16*, 611. [[CrossRef](#)]
5. Condon, A.; Buscarino, B.; Moch, E.; Schnert, W.J.; Miles, O.; Herring, P.K.; Attia, P.M. A Dataset of over One Thousand Computed Tomography Scans of Battery Cells. *Data Brief* **2024**, *55*, 110614. [[CrossRef](#)]
6. Waldmann, T.; Gorse, S.; Samtleben, T.; Schneider, G.; Knoblauch, V.; Wohlfahrt-Mehrens, M. A Mechanical Aging Mechanism in Lithium-Ion Batteries. *J. Electrochem. Soc.* **2014**, *161*, A1742–A1747. [[CrossRef](#)]
7. Finegan, D.P.; Scheel, M.; Robinson, J.B.; Tjaden, B.; Hunt, I.; Mason, T.J.; Millichamp, J.; Di Michiel, M.; Offer, G.J.; Hinds, G.; et al. *In-Operando* High-Speed Tomography of Lithium-Ion Batteries during Thermal Runaway. *Nat. Commun.* **2015**, *6*, 6924. [[CrossRef](#)]
8. Finegan, D.P.; Tudisco, E.; Scheel, M.; Robinson, J.B.; Taiwo, O.O.; Eastwood, D.S.; Lee, P.D.; Michiel, M.D.; Bay, B.; Hall, S.A.; et al. Quantifying Bulk Electrode Strain and Material Displacement within Lithium Batteries via High-Speed Operando Tomography and Digital Volume Correlation. *Adv. Sci.* **2016**, *3*, 1500332. [[CrossRef](#)]
9. Pfrang, A.; Kersys, A.; Kriston, A.; Sauer, D.U.; Rahe, C.; Käbitz, S.; Figgemeier, E. Long-Term Cycling Induced Jelly Roll Deformation in Commercial 18650 Cells. *J. Power Sources* **2018**, *392*, 168–175. [[CrossRef](#)]
10. Carter, R.; Huhman, B.; Love, C.T.; Zenyuk, I.V. X-Ray Computed Tomography Comparison of Individual and Parallel Assembled Commercial Lithium Iron Phosphate Batteries at End of Life after High Rate Cycling. *J. Power Sources* **2018**, *381*, 46–55. [[CrossRef](#)]
11. Kok, M.D.R.; Robinson, J.B.; Weaving, J.S.; Jnawali, A.; Pham, M.; Iacoviello, F.; Brett, D.J.L.; Shearing, P.R. Virtual Unrolling of Spirally-Wound Lithium-Ion Cells for Correlative Degradation Studies and Predictive Fault Detection. *Sustain. Energy Fuels* **2019**, *3*, 2972–2976. [[CrossRef](#)]
12. Pfrang, A.; Kersys, A.; Kriston, A.; Sauer, D.U.; Rahe, C.; Käbitz, S.; Figgemeier, E. Geometrical Inhomogeneities as Cause of Mechanical Failure in Commercial 18650 Lithium Ion Cells. *J. Electrochem. Soc.* **2019**, *166*, A3745–A3752. [[CrossRef](#)]
13. Carter, R.; Klein, E.J.; Atkinson, R.W.; Love, C.T. Mechanical Collapse as Primary Degradation Mode in Mandrel-Free 18650 Li-Ion Cells Operated at 0 °C. *J. Power Sources* **2019**, *437*, 226820. [[CrossRef](#)]
14. Willenberg, L.K.; Dechent, P.; Fuchs, G.; Teuber, M.; Eckert, M.; Graff, M.; Kürten, N.; Sauer, D.U.; Figgemeier, E. The Development of Jelly Roll Deformation in 18650 Lithium-Ion Batteries at Low State of Charge. *J. Electrochem. Soc.* **2020**, *167*, 120502. [[CrossRef](#)]
15. Ziesche, R.F.; Arlt, T.; Finegan, D.P.; Heenan, T.M.M.; Tengattini, A.; Baum, D.; Kardjilov, N.; Markötter, H.; Manke, I.; Kockelmann, W.; et al. 4D Imaging of Lithium-Batteries Using Correlative Neutron and X-Ray Tomography with a Virtual Unrolling Technique. *Nat. Commun.* **2020**, *11*, 777. [[CrossRef](#)]
16. Cai, Z.; Mendoza, S.; Goodman, J.; McGann, J.; Han, B.; Sanchez, H.; Spray, R. The Influence of Cycling, Temperature, and Electrode Gapping on the Safety of Prismatic Lithium-Ion Batteries. *J. Electrochem. Soc.* **2020**, *167*, 160515. [[CrossRef](#)]
17. Villarraga-Gómez, H.; Begun, D.L.; Bhattacharjee, P.; Mo, K.; Norouzi Rad, M.; White, R.T.; Kelly, S.T. Assessing Rechargeable Batteries with 3D X-Ray Microscopy, Computed Tomography, and Nanotomography. *Nondestruct. Test. Eval.* **2022**, *37*, 519–535. [[CrossRef](#)]
18. Kok, M.D.R.; Jnawali, A.; Heenan, T.M.M.; Tranter, T.G.; Brett, D.J.L.; Shearing, P.R.; Robinson, J.B. Tracking the Lifecycle of a 21700 Cell: A 4D Tomography and Digital Disassembly Study. *J. Electrochem. Soc.* **2023**, *170*, 090502. [[CrossRef](#)]
19. Fordham, A.; Milojevic, Z.; Giles, E.; Du, W.; Owen, R.E.; Michalik, S.; Chater, P.A.; Das, P.K.; Attidekou, P.S.; Lambert, S.M.; et al. Correlative Non-Destructive Techniques to Investigate Aging and Orientation Effects in Automotive Li-Ion Pouch Cells. *Joule* **2023**, *7*, 2622–2652. [[CrossRef](#)]
20. Pfrang, A.; Kersys, A.; Kriston, A.; Scurtu, R.-G.; Marinaro, M.; Wohlfahrt-Mehrens, M. Deformation from Formation Until End of Life: Micro X-Ray Computed Tomography of Silicon Alloy Containing 18650 Li-Ion Cells. *J. Electrochem. Soc.* **2023**, *170*, 030548. [[CrossRef](#)]
21. Jnawali, A.; Kok, M.D.R.; Krishna, M.; Varnosfaderani, M.A.; Brett, D.J.L.; Shearing, P.R. Evaluating Long-Term Cycling Degradation in Cylindrical Li-Ion Batteries Using X-Ray Tomography and Virtual Unrolling. *J. Electrochem. Soc.* **2023**, *170*, 090540. [[CrossRef](#)]
22. Jiang, J.; Liu, X.; Li, X.; Yang, R. Mapping Internal Deformation in 4695 Batteries through a Combination of X-Ray Computer Tomography and Machine Learning. *J. Power Sources* **2024**, *621*, 235130. [[CrossRef](#)]
23. Ha, Y.; Licht, R.B.; Bogart, T.D.; Beers, K.M. Bridging the Gap between Academic and Industry Li-Ion Battery Research. *Front. Batter. Electrochem.* **2024**, *2*, 1287887. [[CrossRef](#)]
24. Li, L.; Hou, J. Capacity Detection of Electric Vehicle Lithium-Ion Batteries Based on X-Ray Computed Tomography. *RSC Adv.* **2018**, *8*, 25325–25333. [[CrossRef](#)]
25. Kong, L.; Aalund, R.; Alipour, M.; Stiliarov, S.I.; Pecht, M. Evaluating the Manufacturing Quality of Lithium Ion Pouch Batteries. *J. Electrochem. Soc.* **2022**, *169*, 040541. [[CrossRef](#)]
26. Yufit, V.; Shearing, P.; Hamilton, R.W.; Lee, P.D.; Wu, M.; Brandon, N.P. Investigation of Lithium-Ion Polymer Battery Cell Failure Using X-Ray Computed Tomography. *Electrochem. Commun.* **2011**, *13*, 608–610. [[CrossRef](#)]

27. Brenner, D.J.; Elliston, C.D.; Hall, E.J.; Berdon, W.E. Estimated Risks of Radiation-Induced Fatal Cancer from Pediatric CT. *Am. J. Roentgenol.* **2001**, *176*, 289–296. [CrossRef]
28. Shi, L.; Tashiro, S. Estimation of the Effects of Medical Diagnostic Radiation Exposure Based on DNA Damage. *J. Radiat. Res.* **2018**, *59*, ii121–ii129. [CrossRef]
29. Xu, K. Interfaces and Interphases in Batteries. *J. Power Sources* **2023**, *559*, 232652. [CrossRef]
30. Ortiz, D.; Steinmetz, V.; Durand, D.; Legand, S.; Dauvois, V.; Maître, P.; Le Caér, S. Radiolysis as a Solution for Accelerated Ageing Studies of Electrolytes in Lithium-Ion Batteries. *Nat. Commun.* **2015**, *6*, 6950. [CrossRef]
31. Tan, C.; Lyons, D.J.; Pan, K.; Leung, K.Y.; Chuirazzi, W.C.; Canova, M.; Co, A.C.; Cao, L.R. Radiation Effects on the Electrode and Electrolyte of a Lithium-Ion Battery. *J. Power Sources* **2016**, *318*, 242–250. [CrossRef]
32. Levieux-Soudi, Y.; Martin, J.; Moreau, P.; Herlin-Boime, N.; Le Caér, S. Radiolysis of Electrolytes in Batteries: A Quick and Efficient Screening Process for the Selection of Electrolyte-Additive Formulations. *Small Methods* **2022**, *6*, 2200712. [CrossRef] [PubMed]
33. Gao, Y.; Qiao, F.; Hou, W.; Ma, L.; Li, N.; Shen, C.; Jin, T.; Xie, K. Radiation Effects on Lithium Metal Batteries. *Innovation* **2023**, *4*, 100468. [CrossRef] [PubMed]
34. Edström, K.; Herstedt, M.; Abraham, D.P. A New Look at the Solid Electrolyte Interphase on Graphite Anodes in Li-Ion Batteries. *J. Power Sources* **2006**, *153*, 380–384. [CrossRef]
35. Verma, P.; Maire, P.; Novák, P. A Review of the Features and Analyses of the Solid Electrolyte Interphase in Li-Ion Batteries. *Electrochim. Acta* **2010**, *55*, 6332–6341. [CrossRef]
36. Schroder, K.W.; Celio, H.; Webb, L.J.; Stevenson, K.J. Examining Solid Electrolyte Interphase Formation on Crystalline Silicon Electrodes: Influence of Electrochemical Preparation and Ambient Exposure Conditions. *J. Phys. Chem. C* **2012**, *116*, 19737–19747. [CrossRef]
37. Lin, F.; Markus, I.M.; Doeff, M.M.; Xin, H.L. Chemical and Structural Stability of Lithium-Ion Battery Electrode Materials under Electron Beam. *Sci. Rep.* **2014**, *4*, 5694. [CrossRef]
38. Unocic, R.R.; Sun, X.-G.; Sacci, R.L.; Adamczyk, L.A.; Alsem, D.H.; Dai, S.; Dudney, N.J.; More, K.L. Direct Visualization of Solid Electrolyte Interphase Formation in Lithium-Ion Batteries with In Situ Electrochemical Transmission Electron Microscopy. *Microsc. Microanal.* **2014**, *20*, 1029–1037. [CrossRef]
39. Li, Y.; Li, Y.; Pei, A.; Yan, K.; Sun, Y.; Wu, C.-L.; Joubert, L.-M.; Chin, R.; Koh, A.L.; Yu, Y.; et al. Atomic Structure of Sensitive Battery Materials and Interfaces Revealed by Cryo-Electron Microscopy. *Science* **2017**, *358*, 506–510. [CrossRef]
40. Huang, W.; Attia, P.M.; Wang, H.; Renfrew, S.E.; Jin, N.; Das, S.; Zhang, Z.; Boyle, D.T.; Li, Y.; Bazant, M.Z.; et al. Evolution of the Solid–Electrolyte Interphase on Carbonaceous Anodes Visualized by Atomic-Resolution Cryogenic Electron Microscopy. *Nano Lett.* **2019**, *19*, 5140–5148. [CrossRef]
41. Nelson, J.; Yang, Y.; Misra, S.; Andrews, J.C.; Cui, Y.; Toney, M.F. *Identifying and Managing Radiation Damage During in Situ Transmission X-Ray Microscopy of Li-Ion Batteries*; Lai, B., Ed.; SPIE: San Diego, CA, USA, 2013.
42. Borkiewicz, O.J.; Wiaderek, K.M.; Chupas, P.J.; Chapman, K.W. Best Practices for Operando Battery Experiments: Influences of X-Ray Experiment Design on Observed Electrochemical Reactivity. *J. Phys. Chem. Lett.* **2015**, *6*, 2081–2085. [CrossRef] [PubMed]
43. Lim, C.; Kang, H.; De Andrade, V.; De Carlo, F.; Zhu, L. Hard X-Ray-Induced Damage on Carbon–Binder Matrix for *in Situ* Synchrotron Transmission X-Ray Microscopy Tomography of Li-Ion Batteries. *J. Synchrotron Radiat.* **2017**, *24*, 695–698. [CrossRef] [PubMed]
44. Bras, W.; Myles, D.A.A.; Felici, R. When X-Rays Alter the Course of Your Experiments. *J. Phys. Condens. Matter* **2021**, *33*, 423002. [CrossRef]
45. Li, M.; Liu, W.; Luo, D.; Chen, Z.; Amine, K.; Lu, J. Evidence of Morphological Change in Sulfur Cathodes upon Irradiation by Synchrotron X-Rays. *ACS Energy Lett.* **2022**, *7*, 577–582. [CrossRef]
46. Blondeau, L.; Surblé, S.; Foy, E.; Khodja, H.; Belin, S.; Gauthier, M. Are Operando Measurements of Rechargeable Batteries Always Reliable? An Example of Beam Effect with a Mg Battery. *Anal. Chem.* **2022**, *94*, 9683–9689. [CrossRef]
47. Christensen, C.K.; Karlsen, M.A.; Drejer, A.Ø.; Andersen, B.P.; Jakobsen, C.L.; Johansen, M.; Sørensen, D.R.; Kantor, I.; Jørgensen, M.R.V.; Ravnsbæk, D.B. Beam Damage in Operando X-Ray Diffraction Studies of Li-Ion Batteries. *J. Synchrotron Radiat.* **2023**, *30*, 561–570. [CrossRef]
48. Jousseaume, T.; Colin, J.-F.; Chandresris, M.; Lyonnard, S.; Tardif, S. How Beam Damage Can Skew Synchrotron *Operando* Studies of Batteries. *ACS Energy Lett.* **2023**, *8*, 3323–3329. [CrossRef]
49. Black, A.P.; Escudero, C.; Fauth, F.; Fehse, M.; Agostini, G.; Reynaud, M.; Houdeville, R.G.; Chatzogiannakis, D.; Orive, J.; Ramo-Irurre, A.; et al. Beam Effects in Synchrotron Radiation *Operando* Characterization of Battery Materials: X-Ray Diffraction and Absorption Study of $\text{LiNi}_{0.33}\text{Mn}_{0.33}\text{Co}_{0.33}\text{O}_2$ and LiFePO_4 Electrodes. *Chem. Mater.* **2024**, *36*, 5596–5610. [CrossRef]
50. Lethal Dose. 2019. Available online: <https://www.euronuclear.org/glossary/lethal-dose/> (accessed on 20 January 2025).
51. Maleki, H.; Hallaj, S.A.; Selman, J.R.; Dinwiddie, R.B.; Wang, H. Thermal Properties of Lithium-Ion Battery and Components. *J. Electrochem. Soc.* **1999**, *146*, 947. [CrossRef]

52. Ravdel, B.; Abraham, K.M.; Gitzendanner, R.; DiCarlo, J.; Lucht, B.; Campion, C. Thermal Stability of Lithium-Ion Battery Electrolytes. *J. Power Sources* **2003**, *119–121*, 805–810. [[CrossRef](#)]
53. Bandhauer, T.M.; Garimella, S.; Fuller, T.F. A Critical Review of Thermal Issues in Lithium-Ion Batteries. *J. Electrochem. Soc.* **2011**, *158*, R1–R25. [[CrossRef](#)]
54. Drake, S.J.; Wetz, D.A.; Ostaneck, J.K.; Miller, S.P.; Heinzel, J.M.; Jain, A. Measurement of Anisotropic Thermophysical Properties of Cylindrical Li-Ion Cells. *J. Power Sources* **2014**, *252*, 298–304. [[CrossRef](#)]
55. Willemink, M.J.; Noël, P.B. The Evolution of Image Reconstruction for CT—From Filtered Back Projection to Artificial Intelligence. *Eur. Radiol.* **2019**, *29*, 2185–2195. [[CrossRef](#)] [[PubMed](#)]
56. Attia, P.M.; Bills, A.; Planella, F.B.; Dechent, P.; dos Reis, G.; Dubarry, M.; Gasper, P.; Gilchrist, R.; Greenbank, S.; Howey, D.; et al. Review—“Knees” in Lithium-Ion Battery Aging Trajectories. *J. Electrochem. Soc.* **2022**, *169*, 060517. [[CrossRef](#)]
57. BS 4094-2:1971; Recommendation for Data on Shielding from Ionizing Radiation — Shielding from X-Radiation. BSI Knowledge: London, UK, 1971. Available online: <https://knowledge.bsigroup.com/products/recommendation-for-data-on-shielding-from-ionizing-radiation-shielding-from-x-radiation?version=standard> (accessed on 6 September 2024).
58. Poludniowski, G.; Omar, A.; Bujila, R.; Andreo, P. Technical Note: SpekPy v2.0—A Software Toolkit for Modeling x-Ray Tube Spectra. *Med. Phys.* **2021**, *48*, 3630–3637. [[CrossRef](#)]

Disclaimer/Publisher’s Note: The statements, opinions and data contained in all publications are solely those of the individual author(s) and contributor(s) and not of MDPI and/or the editor(s). MDPI and/or the editor(s) disclaim responsibility for any injury to people or property resulting from any ideas, methods, instructions or products referred to in the content.